Optical Materials 134 (2022) 113166

Contents lists available at ScienceDirect

Optical Materials

journal homepage: www.elsevier.com/locate/optmat

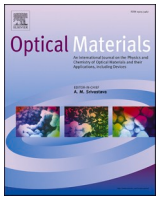

Review article

$SrW_{(1-x)}Mo_xO_4$ solid solutions: Modulation of structural and photoluminescent properties and white light emission

L.X. Lovisa [a,*], D.F. Dos Santos [b], A.A.G. Santiago [b], M. Siu Li [c], E. Longo [d], M.R.D. Bomio [b], F.V. Motta [b]

[a] Institute of Physics and Chemistry, Federal University of Itajubá (UNIFEI), Itajubá, MG, 37500-903, Brazil
[b] LSQM – Laboratory of Chemical Synthesis of Materials – Department of Materials Engineering, Federal University of Rio Grande Do Norte, P.O. Box 1524, 59078-900, Natal, RN, Brazil
[c] IFSC, USP, Av. Trabalhador São Carlense, 400, CEP, 13566-590, São Carlos, SP, Brazil
[d] CDMF-LIEC, UFSCar, P.O. Box 676, 13565-905, São Carlos, SP, Brazil

ARTICLE INFO

Keywords:
$SrW_{(1-x)}Mo_xO_4$
Solid solution
White emissions
Energy transfer (ET)
Phosphor

ABSTRACT

$SrW_{(1-x)}Mo_xO_4$ (x = 0, 0.25, 0.5, 0.75, 1) inorganic phosphors were synthesized by the microwave-hydrothermal method (MHM). Structural changes are evaluated by changes in the crystal lattice parameters of $SrW_{(1-x)}Mo_xO_4$ solid solution. The $SrWO_4 \rightarrow SrMoO_4$ transition occurs gradually, observing an evolution of the $\nu 2(Ag)^{\bullet}$ (at 918 cm^{-1}) active mode in opposition to the decrease of the $\nu 2(Ag)^{\blacklozenge}$ (at 884 cm^{-1}) mode by the Raman spectra. The color quality of the phosphors and the photometric parameters were estimated using the spectral energy distribution functions of the $SrW_{(1-x)}Mo_xO_4$ phosphors. The adjustment in chemical composition by the W:Mo molar ratio enabled producing adjustable optical properties. A transition in the emission characteristics of the color (blue → yellow → white) was observed. This versatility seen in phosphors is well accepted when it comes to the development of multifunctional materials.

1. Introduction

Recent advances in solid state lighting have enabled improvements in the synthesis of materials applied to photoluminescence as a way of responding to the requirements demanded by society. The qualification of these materials goes through criteria which take into account energy efficiency factors supported by a committed socio-environmental responsibility policy [1,2]. In this context, white light-emitting diodes converted to phosphorus (pc-WLEDs) have gained attention for their performance in terms of high luminous efficiency, being ecologically correct, economically viable and providing a long service life when compared to conventional incandescent lamps [3–5].

The history of producing WLEDs involving semiconductors states that the first blue LED, a red emitter and a green emission phosphor, was obtained by the Nichia Company in 1996 [6–9]. Another advance in the process was the use of an InGaN Chip (blue emission) and a YAG: Ce^{3+} phosphor (yellow emission) to produce WLEDs. This material showed chemical and optical stability, as well as optical absorption in blue [10]. However, an unfavorable factor was the low efficiency in red emission exhibited by the YAG: Ce^{3+}, which results in a highly correlated color temperature (CCT) and a low color rendering index (CRI) [11,12]. The process of doping simultaneously with different rare earth ions in inorganic matrices was also developed to manufacture WLEDs since rare earth ions present well-defined f-f emissions in different visible ranges. However, the high cost of these dopants and the damage to the environment associated with their usage are conditions which need to be considered [13,14]. Thus, the need arises to investigate new routes aiming at producing materials with desirable structural, morphological and photoluminescent characteristics for applications in optical devices [15]. These properties are achieved by controlling the experimental parameters in the stoichiometric control.

Tungstate and molybdate material classes are considered excellent host matrices for introducing rare earth ions due to their physicochemical properties [16,17]. In particular, strontium tungstate ($SrWO_4$) and strontium molybdate ($SrMoO_4$) belong to the scheelites group. As described by N. Najafvandzadeh et al. [18], the scheelite structure is characterized by the spatial group *I41/a*, point group C_{4h} *(4/m)* and tetragonal crystalline system. Sr^{2+} cations have coordination number 8 in a dodecahedric approach, and W^{6-} and Mo^{6-} cations have coordination 4 in a tetrahedral approach in relation to oxygen.

* Corresponding author.
E-mail address: lauraengmat@hotmail.com (L.X. Lovisa).

https://doi.org/10.1016/j.optmat.2022.113166
Received 3 July 2022; Received in revised form 12 October 2022; Accepted 20 October 2022
Available online 29 October 2022

The satisfactory performance of tungstates and molybdates in optical device applications is directly related to the thermochemical stability, absorption in the ultraviolet range and broadband blue emission properties [19]. This combination of properties enables tungstates and molybdates to possess promising possibilities in developing photoluminescent materials as presented in the following works [20–23].

Solid solutions are options to adjust characteristics obtained from the mixture of two or more crystalline solids as a way to enhance the properties of materials. This proposal is intended to modulate structural, vibrational, morphological and optical aspects due to changes in chemical composition [15,23,24]. Within this context, this work aimed to synthesize, characterize and evaluate the photoluminescent properties of $SrW_{(1-x)}Mo_xO_4$ particles obtained by the microwave-assisted hydrothermal method.

2. Experimental

2.1. Materials

Sodium molybdenum oxide dihydrate ($Na_2MoO_4 \bullet 2H_2O$, 98%, Alfa Aesar), sodium tungsten oxide dihydrate ($Na_2WO_4 \bullet 2H_2O$, 95%, Alfa Aesar), strontium nitrate ($Sr(NO_3)_2$, 99%, Alfa Aesar), nitric acid (HNO_3, 65%, Synth), ammonium hydroxide (NH_4OH, 24%, Synth) and distilled water were used as received to prepare the $SrW_{(1-x)}Mo_xO_4$ particles.

2.2. Synthesis

Two precursor solutions were prepared for the synthesis of the $SrW_{(1-x)}Mo_xO_4$ particles: one containing molybdenum (solution A) and the other containing tungsten (solution B), with molar ratios (W:Mo) of 1:0, 0.75:0.25, 0.50:0.50, 0.25:0.75, 0:1. The starting reagent was dissolved in 40 ml of distilled water for both solutions. Solution B was added to solution A by dripping and under constant magnetic stirring. Stoichiometrically weighed strontium was added after complete dissolution. Finally, NH_4OH was added to the solution to stabilize its pH at 8 observing the formation of precipitate. The mixture was transferred into a Teflon autoclave, which was sealed and placed into a microwave-hydrothermal system (2.45 GHz, maximum power of 800 W). The microwave-hydrothermal conditions were kept at 120 °C for 20 min with a heating rate fixed at 3 °C/min. The pressure in the autoclave was stabilized at 3.0 atm. After the microwave-hydrothermal treatment, the autoclave was cooled to room temperature. The resulting solution was washed with deionized water several times, and the white precipitates were collected. The obtained powders were then dried in a conventional furnace at 100 °C for 24 h.

2.3. Characterization

The $SrW_{(1-x)}Mo_xO_4$ particles were structurally characterized by XRD using a Shimadzu XRD 7000 instrument with CuKα radiation (λ = 1.5406 Å) in the 2θ range of 10–80° at a scan rate of 0.02 s^{-1}. Raman spectroscopy measurements were recorded using a T-64000 triple monochromator spectrometer (Jobin-Yvon, France) coupled to a CCD detector. The spectroscopy was performed using a 514.5 nm wavelength of an argon ion laser, keeping its maximum output power at 8 mW. The morphologies were investigated using scanning electron microscopy (SEM) (Carl Zeiss, Supra 35- VP Model, Germany) operated at 6 kV. The UV–vis diffuse reflectance spectrum was measured at room temperature using a UV–vis spectrometer. The photoluminescence (PL) spectra were acquired using an Ash Monospec 27 monochromator (Thermal Jarrel, U. S.A.) and a R4446 photomultiplier (Hamamatsu Photonics, U.S.A.). The 325 nm beam of a krypton ion laser (Coherent Innova 90 K) was used as the excitation source with an output of approximately 13.3 mW. All measurements were performed at room temperature.

3. Results

3.1. XRD

Fig. 1 shows the XRD analysis results for the $SrW_{(1-x)}Mo_xO_4$ samples. It is observed that the peaks identified in the diffractograms are in accordance with the JCPDS No. 85–0586 ($SrMoO_4$) and JCPDS No. 85–0587 ($SrWO_4$). The $SrW_{(1-x)}Mo_xO_4$ solid solution has a tetragonal structure with *I41/a* spatial group [25]. The solid solution formation was favored by the following factors: (**i**) the ionic radii values of Mo^{6+} (0.41 Å) and W^{6+} (0.42 Å) were very similar; and (**ii**) the cations have the same electronic charge. The gradual substitution between the $W^{6+} \rightarrow Mo^{6+}$ cations was successful. The structural evolution of the material was to obtain a single-phase material with small variations in the lattice parameters resulting from microdeformations originated from the synthesis process.

The main plane (112) presents a displacement of 0.10° for larger dispersion angles considering the transition: $SrWO_4$ (27.78°) → $SrMoO_4$ (27.75°). The referred plane for the $SrW_{(1-x)}Mo_xO_4$ solid solution samples does not present any displacement (27.75°), taking into account coordinated adjustments between the $[WO_4]^{2-}$ and $[MoO_4]^{2-}$ clusters in the $SrW_{(1-x)}Mo_xO_4$. The high amplitude diffraction planes indicate that the synthesized $SrW_{(1-x)}Mo_xO_4$ was well crystallized. The average crystallite sizes were estimated by the Scherrer equation considering the main plane (112) for the calculations.

Fig. S1 illustrates the Rietveld refinement graph of the $SrW_{(1-x)}Mo_xO_4$ samples obtained by MHM. The $SrW_{(1-x)}Mo_xO_4$ structure parameters, unit cell volume, bond length and bond angles were obtained and calculated by the Rietveld refinement method using the GSAS (General Structure Analysis System) program with graphical interface EXPGUI [26]. It is possible to estimate an approximation of the structural model to a real structure from measurements of the powder intensity profile through the Rietveld refinement analysis. The result of the presented theoretical adjustment indicates good agreement with such analysis, in which small differences in the intensity scale close to zero can be observed, as illustrated by the line (Exp - Calc). The lattice parameters, such as unit cell volume and crystallite size obtained through the Rietveld refinement of the $SrW_{(1-x)}Mo_xO_4$ samples, as well as the quality coefficients of the refinement (R_p, Rf^2, X^2) can be found in Table 1. These parameters are listed in Table 1 and suggest that the measured diffraction patterns are in good agreement with the ICSD entry No. 99089. For a detailed understanding of the structural changes that occurred with the formation of the $SrW_{(1-x)}Mo_xO_4$ solid solution, Fig. S1 illustrates the

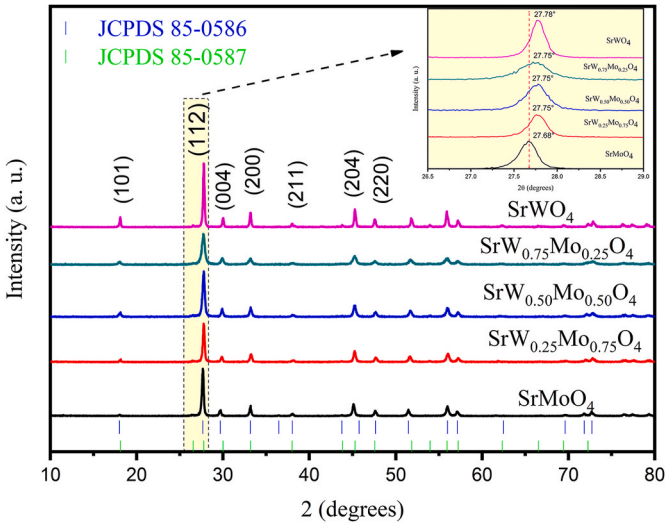

Fig. 1. XRD patterns of (a) $SrW_{(1-x)}Mo_xO_4$ samples and peak displacement of the (112).

Table 1
Lattice parameters, crystallite size, microdeformation and quality coefficients of the Rietveld refinement for $SrW_{(1-x)}Mo_xO$ and $Sr_{(1-y)}Eu_yM_{0.5}W_{0.5}O$ samples.

Sample	$SrWO_4$	$Sr\ W_{0.75}\ Mo_{0.25}\ O_4$	$SrW_{0.5}Mo_{0.5}O_4$	$SrW_{0.25}Mo_{0.75}\ O_4$	$SrMoO_4$
System	Tetragonal	Tetragonal	Tetragonal	Tetragonal	Tetragonal
Space group	I41/a	I41/a	I41/a	I41/a	I41/a
a = b (Å)	5.42	5.41	5.40	5.40	5.40
c (Å)	11.95	11.98	11.99	12.01	12.03
c/a	2.21	2.21	2.22	2.22	2.23
V ($Å^3$)	351.3	351.0	350.7	350.7	351.1
D (nm)	37	15	23	22	39
ϵ ($x10^{-3}$)	0.64	1.62	1.03	1.69	0.62
X^2	1.30	1.61	1.92	1.97	1.95
R_p (%)	12.81	7.73	8.31	10.01	18.37
Rf^2 (%)	9.43	7.63	8.42	8.88	22.87

Rietveld refinement plot of $SrW_{(1-x)}Mo_xO_4$ samples and Table 1 shows all parameters (unit cell volume, bond length and bond angles) calculated by the Rietveld refinement method using the GSAS (General Structure Analysis System) program with EXPGUI graphical interface [26]. The quality parameters obtained by the Rietveld refinement analysis are within acceptable values, thereby being a close representation between the real structure of the sample and the theoretical structure used in the study (ICSD no. 99089).

Small changes in the lattice parameters associated with the substitution of $Wo^{6+} \rightarrow Mo^{6+}$ in the solid $SrW_{(1-x)}Mo_xO_4$ solution were observed. In addition, some modifications in $SrW_{(1-x)}Mo_xO_4$ samples were found, resulting in a variation in the crystallite size and distortions of the clusters. The substitution of $Wo^{6+} \rightarrow Mo^{6+}$ produces changes in the atomic coordinates of the oxygen atoms, as shown in Table S1. These variations signal the presence of structural and electronic distortions in the $[WO_4]$, $[MoO_4]$ and $[SrO_8]$ clusters.

According to the structural analyzes of the samples, the variation in the relationship between the "*a*" and "*c*" lattice parameters of the scheelite structure tetragonal system showed a linear correlation as a function of chemical composition. The transformation of $SrWO_4$ into $SrMoO_4$ was accompanied by a decrease in the tetragonality factor, according to the values in Table 1. Therefore, this result is in accordance with Vegard's law, indicating that the proposed processing method is satisfactory to produce solid $SrW_{(1-x)}Mo_xO_4$ solutions throughout the $SrWoO_4$-$SrMoO_4$ binary system.

The initial cell and atomic position parameters used in the optimization process were taken from the Rietveld refinement results of $SrW_{(1-x)}Mo_xO_4$. The scheelite structure is characterized by strontium atoms bonded to eight oxygen atoms, resulting in $[SrO_8]$ clusters, and the molybdenum or tungsten atoms coordinated to four oxygen atoms in a tetrahedral configuration (i.e. forming $[WO_4]$ or $[MoO_4]$ cluster). Next, the unit cells of each sample from the lattice parameter and atomic coordinate data obtained in the Rietveld refinement (Table S1) were modeled using the VESTA program [27], as shown in Fig. S2.

3.2. Raman

Fig. 2 show the Raman spectra in the range between 100 and 1000 cm^{-1} for the $SrW_{(1-x)}Mo_xO_4$ samples, respectively. There are eight vibrations recorded in Table S2 of the Supplementary Material. The $\nu_2(A_g)^{\blacklozenge}$ (at 884 cm^{-1}) and $\nu_2(A_g)^{\bullet}$ (at 918 cm^{-1}) modes are associated with $[WO_4]^{2-}$ and $[MoO_4]^{2-}$ vibration modes, respectively [28]. Certifying the results presented in the XRD, it is observed (in inset Fig. 4) that there are variations in the Raman bands in the region between 880 and 950 cm^{-1} for the $SrWO_4$ and $SrMoO_4$ samples correlated to the respective $\nu_2(A_g)^{\blacklozenge}$ and $\nu_2(A_g)^{\bullet}$ vibration modes. These vibration modes are due to the formation of W^{6+} (or Mo^{6+}) covalent bonds and O^{2-} ions in the $[WO_4]^{2-}$ and $[MoO_4]^{2-}$ tetrahedra, which alters the efficient mass of the oscillating atoms [29].

Two high-frequency bands centered at 884 cm^{-1} for $SrMoO_4$ and 920 cm^{-1} for $SrWO_4$ are also present in $SrW_{(1-x)}Mo_xO_4$ solid solutions,

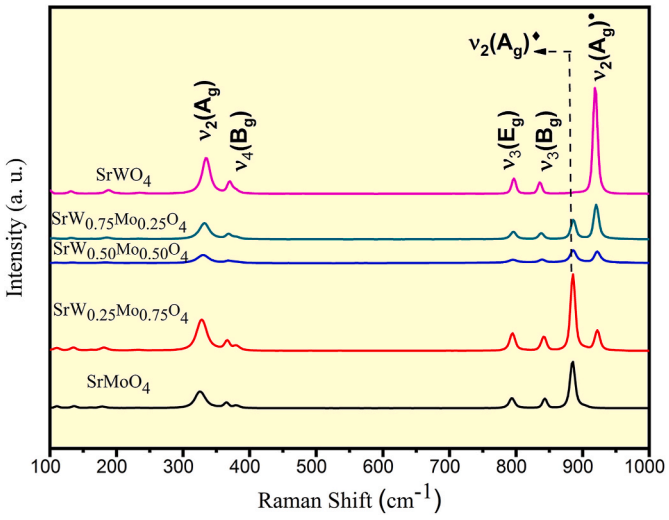

Fig. 2. Raman spectra of $SrW_{(1-x)}Mo_xO_4$ particles.

which correspond to intense peaks in the Raman (Ag) mode and are assigned to the symmetric stretching $\nu_2(A_g)$ of the bonds [←O←M→O→] (M = W and Mo), while the two Raman (Bg and Eg internal) modes at 841 and 792 cm^{-1} are attributed to the asymmetric stretching v_3(F2) of the bonds (→O→M→O→), as described by Lovisa et al. in a study on $SrWo_{0.5}Mo_{0.5}O_4$: Eu^{3+} [28]. The small evolution of this wavenumber (884 cm^{-1}) in the scheelite solid solution as Mo ions increase is connected with the formation of Sr–O–Mo links in increasing proportion and local modifications of $[SrO_8–MoO_4]$ structural groups due to the substitution of W^{6+} by Mo^{6+} ions.

Next, a quantitative analysis performed by Raman spectroscopy for the $SrW_{(1-x)}Mo_xO_4$ solid solution samples was used to estimate how much of each component present ($SrWO_4$ and $SrMoO_4$) constitutes each sample. Thus, areas of the $\nu2(Ag)^{\blacklozenge}$ (at 884 cm^{-1}) and $\nu2(Ag)^{\bullet}$ (at 918 cm^{-1}) bands corresponding to $SrWO_4$ and $SrMoO_4$, respectively, were integrated to estimate these values. The values obtained from the I_1/I_2 ratio of the spectra of Fig. 3 are in agreement with the stoichiometric calculations and the occupancy refinement (Occ.) data in Table S1 in the supplementary material.

The I_1/I_2 values and the stoichiometric indices (calculated) of the Mo^{6+} and Sr^{6+} elements are shown for each chemical composition of the solid solution in Fig. 3. The experimental values are close to the theoretical values. Therefore, it is reasonable to consider that the structural changes occur in a gradual effect as a function of the $W^{6+} \rightarrow Mo^{6+}$ substitution and corroborate the data of the lattice parameters in Table 1.

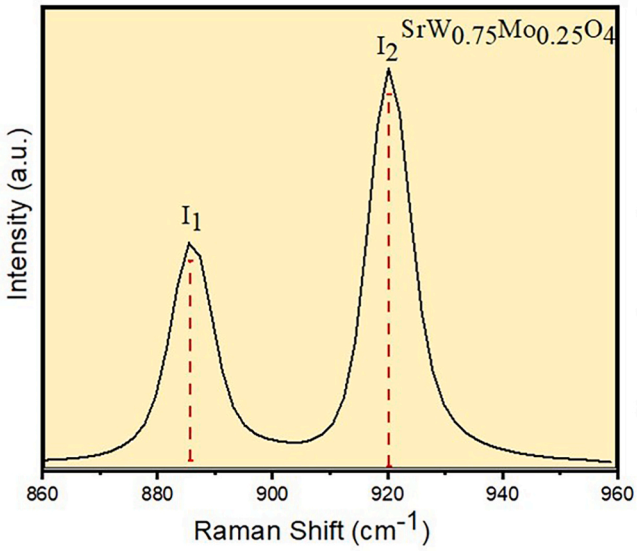

Calculated	*Experimental*
Conc.[Mo^{6+}] = 0.25	I_1 = 0.12
Conc.[W^{6+}] = 0.75	I_2 = 0.32
R^* = 0.33	I_1/I_2 = 0.37

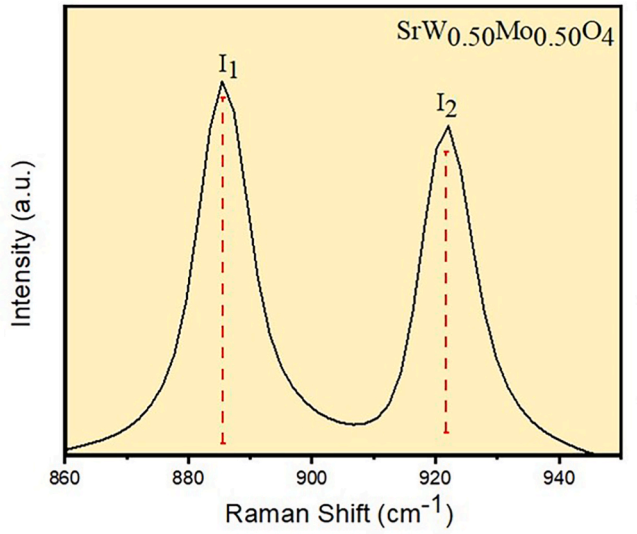

Calculated	*Experimental*
Conc.[Mo^{6+}] = 0.50	I_1 = 0.08
Conc.[W^{6+}] = 0.50	I_2 = 0.07
R^* = 1	I_1/I_2 = 1.1

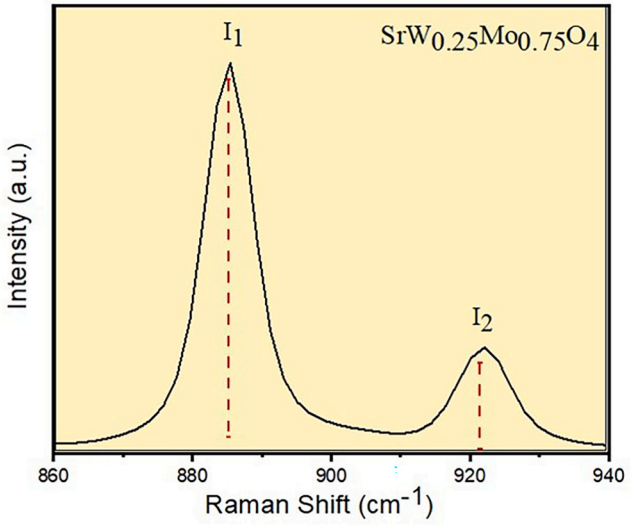

Calculated	*Experimental*
Conc.[Mo^{6+}] = 0.75	I_1 = 0.45
Conc.[W^{6+}] = 0.25	I_2 = 0.14
R^* = 3	I_1/I_2 = 3.2

$R^* = Conc.[Mo^{6+}]/Conc.[W^{6+}]$

Fig. 3. Comparison between the I_1/I_2 values and the stoichiometric indices calculated for W^{6+} and Mo^{6+}.

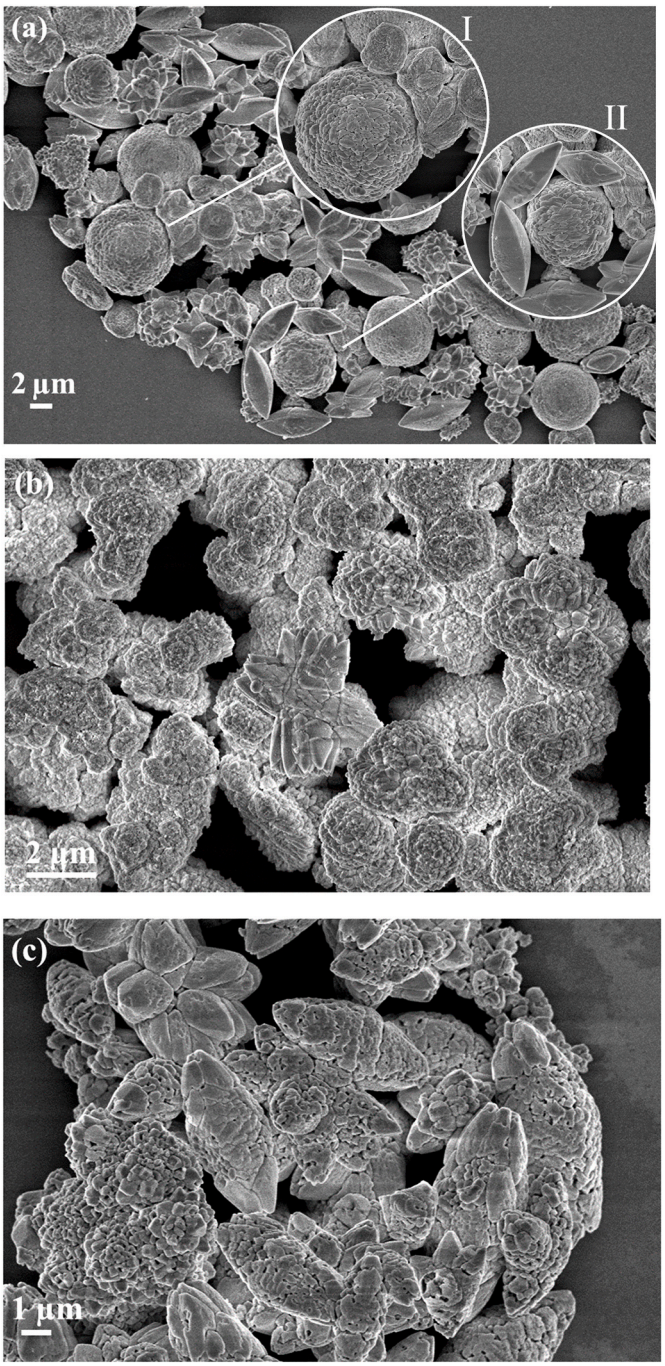

Fig. 4. SEM images of (a) $SrMoO_4$, (b) $SrW_{0.5}Mo_{0.5}O_4$ and (c) $SrWoO_4$ particles.

3.3. Morphological characterization

Fig. 4(a–c) shows SEM images of $SrMoO_4$, $SrW_{0.5}Mo_{0.5}O_4$ and $SrWO_4$ samples. It is possible to observe different types of morphology for the $SrMoO_4$ sample, such as: microrice (L = 5 μm), microflowers (Lp = 1.6 μm) and microspheres (D = 4.6 μm). The morphology of the microflowers is composed by the simultaneous junction of several parts composed of units of petals that are interconnected to a central region. The growth of these crystals occurs in a radial direction from secondary growth mechanisms by the aggregation of new particles, as described by Lovisa et al. [28]. This growth is known as an Ostwald ripening process [30]. Fig. 4(b) represents the morphology of $SrW_{0.5}Mo_{0.5}O_4$. There is a change in the particle morphology as a function of the change in the chemical composition of the samples. There is a predominance of rounded and irregular particles, showing an increase in surface porosity. This porosity is associated with the aggregation of numerous smaller particles. There is small spacing between the interfaces of these nanometric particles, which confers an irregular characteristic and a tendency for disorganized morphological aspects. These significant changes are controlled by the change in chemical composition due to the physical characteristics of W^{6+}. Fig. 4(c) corresponds to the morphology of $SrWO_4$. It is observed that the amorphization process of the particles proceeds with a predominance of the micro-rice morphology. $SrWO_4$ particles have high porosity, presenting an open structure with the presence of numerous surface nanometric pores, such as interconnected pores between the particles.

Regarding the phenomena involving crystal growth, it is possible to consider that the development of crystals takes place in two stages: (i) nucleation, which constitutes the initial state of the process; and (ii) further crystalline growth of these nuclei [31]. A detailed discussion of these aspects was addressed in Ref. [28]. The present work, in agreement with other studies [31–34], argues that the growth of particles originates from the superposition of nanometric particles in the form of a stack in order to minimize the surface energy of the crystals. It is considered that the final particle growth process is the cooperation of two sequenced mechanisms: aggregation and targeted fixation of nanoparticles.

3.4. Analyses of UV–Vis absorption spectroscopy and optical band gap values

Fig. 5(a) represents the diffuse reflectance spectra of $SrW_{(1-x)}Mo_xO_4$ samples obtained between 200 and 800 nm. According to the results, the samples showed an absorption band in the ultraviolet region, attributed to the absorption of the host matrix. The displacement of the absorption band is observed with the increase in the Mo concentration from the substitution of $W^{6+} \rightarrow Mo^{6+}$. The electronic transitions around 280 nm are attributed to electron transfer within the $(WO_4)^{2-}/(MoO_4)^{2-}$ tetrahedrals [35]. The coordination value x of the polyhedron $[MO_x]$ (M = Mo, W) is one of the factors that influences the charge transfer, and as a consequence, the light absorption ability of the materials [36]. A lower energy of charge transfer in the clusters $[MO_x]$ promotes a shift of the absorption edge to a longer wavelength, resulting in a decrease in the gap energy.

The band gap energy values (E_{gap}) were calculated using the Kubelka-Munk Equation [37], which is based on the transformation of diffuse reflectance measurements to precisely estimate E_{gap} values [38]. The Kubelka-Munk Equation (3) for any wavelength is described by:

$$\frac{K}{S} = \frac{(1-R)^2}{2R} = F(R) \quad \text{Eq. (3)}$$

In which: *F(R)* is the Kubelka-Munk function or absolute reflectance of the sample; barium sulfate ($BaSO_4$) was adopted in this work as a standard sample for reflectance measurements (R = Rsample/R ($BaSO_4$)), *R* is the reflectance, *K* is the molar absorption coefficient and *S* is the dispersion coefficient. The band gap and the absorption coefficient of semiconductor oxides can be calculated by Equation (4) [39]:

$$\alpha h\nu = C_1\left(h\nu - E_{gap}\right)^n \quad \text{Eq. (4)}$$

In which: α is the linear absorption coefficient of the material, $h\nu$ is the photon energy, C_1 is a proportionality constant, E_{gap} is the band gap and n is a constant associated with different types of electronic transitions (n = 1/2 for direct allowed, n = 2 for indirect allowed, n = 1.5 for direct prohibited and n = 3 for indirect prohibited). According to theoretical calculations reported in the literature [40], scheelite-type crystals (ABO_4) exhibit an absorption spectrum governed by direct electronic transitions. Fig. 5(b) shows the band gap energy values of the $SrW_{(1-x)}Mo_xO_4$ samples. These values were calculated according to the Tauc relationship and are shown in Table 2.

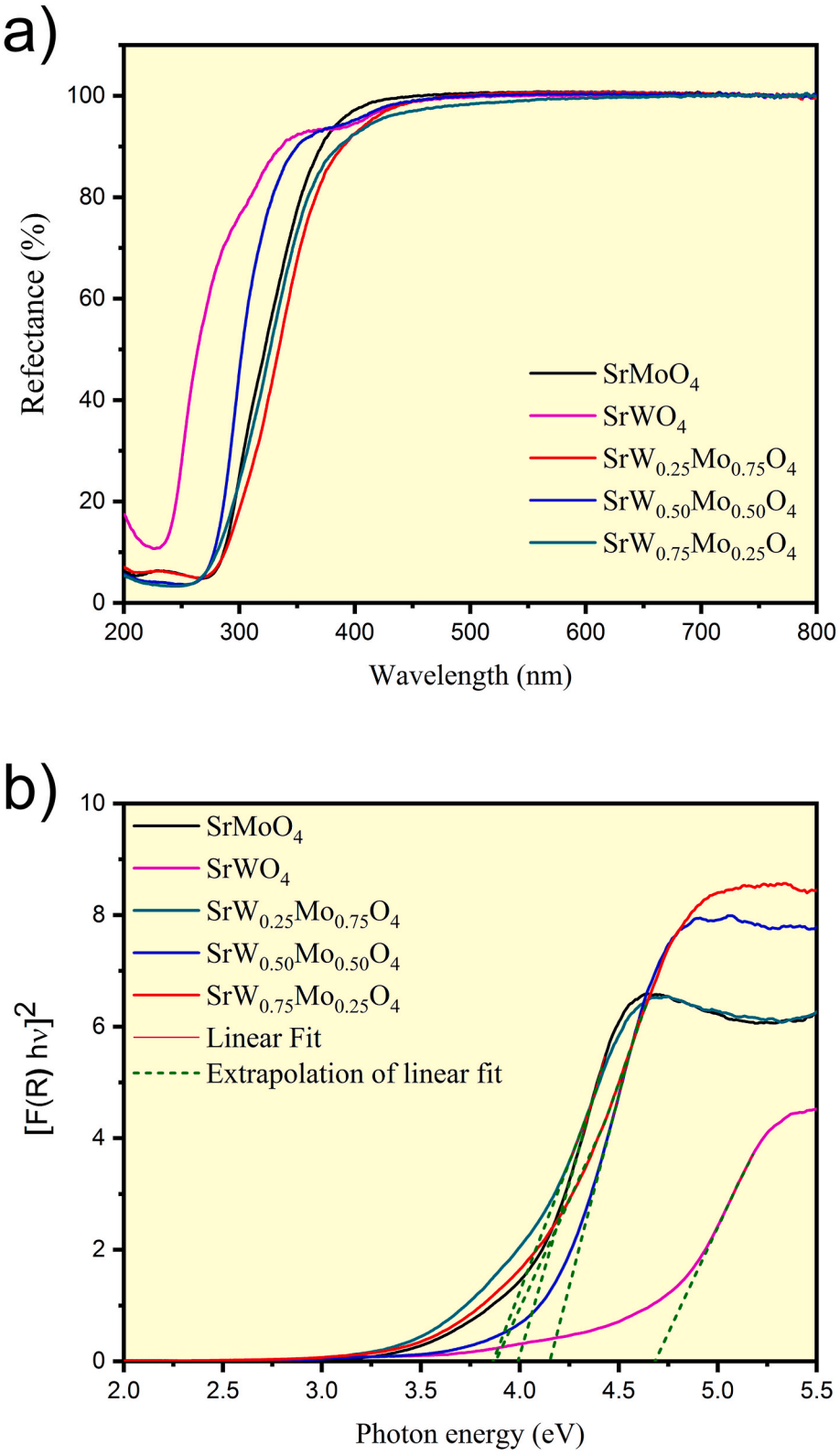

Fig. 5. (a) Diffuse reflection spectra of $SrW_{(1-x)}Mo_xO_4$ samples, (b) band gap energy of (a) $SrW_{(1-x)}Mo_xO_4$ particles.

The structure of electronic bands may change due to the presence of structural defects such as distortions due to elongation or shortening of O-M-O bonds (M = W, Mo), microdeformations resulting from the substitution of cations and the synthesis conditions adopted. Oxygen vacancies are also responsible for the reduction in gap energy from the appearance of intermediate energy levels. Band gap behavior can be justified by the formation of strontium vacancies (V''_{Sr}) and an oxygen-vacancy complex capable of causing three changes in different ways: V_O^x (neutral), $V_O^{\bullet}$ (singly ionized) and $V_O^{\bullet\bullet}$ (doubly ionized). V_O^x are able to donate up to two electrons, $V_O^{\bullet}$ are donors or capture only one electron, and $V_O^{\bullet\bullet}$ are not able to donate electrons, but can receive up to two

Table 2
Gap energy and photometric parameters.

Samples	$SrWO_4$	$SrW_{0.75}Mo_{0.25}O_4$	$SrW_{0.5}Mo_{0.5}O_4$	$SrW_{0.25}M_{0.75}O_4$	$SrMoO_4$
E_{gap} (eV)	4.67	3.90	4.15	4	3.90
CIE (x,y)	(0.28, 0.40)	(0.40, 0.44)	(0.33, 0.40)	(0.39, 0.45)	(0.32, 0.38)
CCT (K)	5598	3879 K	5437 K	4149 K	5478 K
CRI (%)	80	81	80	82	80
Color	Azul	Amarelo	Branco	Amarelo	Branco
LER ($lm.W^{-1}$)	315	319	322	319	318

electrons [28]. Other factors that may influence E_{gap} values are related to the morphology, shape and size of the particles.

3.5. Photoluminescence

Fig. 6 shows the emission spectrum of PL at room temperature, excited at a wavelength (λ_{exc}) of 325 nm. According to the PL emission spectra, the samples showed a characteristic broadband profile that multitransitions involving different energy levels. As the W:Mo ratio is modified, a shift in the bands to longer wavelength regions is also observed. These differences in PL behavior are closely associated with the structural order-disorder relationship of the material in correlation with the physical aspects of the particles (particle morphology and size) and types of structural defects (distortions, electronic defects, surface defects) [41]. The study [42] points out that the physical characteristics of particles, such as morphology and particle size, influence the demand for charge carriers capable of participating in the transition from the valence band to the conduction band. There is inevitably interference in the number of carriers (population) that participate in the photon emission process, and consequently in luminescence variations. Li et al. [43] relate that the characteristic broad band aspect of molybdates is mainly attributed to the $^3T_1$, $^3T_2 \rightarrow {}^1A_1$ transition [44] in the $[MoO_4]^{2-}$ clusters with resulting green emission.

The $W^{6+} \rightarrow Mo^{6+}$ substitution process in $SrWO_4$ for solid solution formation favors strong hybridization of Mo (4d) and O (2p) orbitals if matched with W (5d) and O (2p) for Mo/Wo-O surface bonds. This electronic configuration promotes the efficiency of electron transfer between $[MoO_4]^{2-}$ [45,46] clusters. Gao et al. [47] assigned the ground state of Scheelite structures to the $^1A_1$ energy level and the excited states to four levels, namely: ^1A ($^1T_1$), ^1E ($^1T_1$), ^1E ($^1T_2$), and ^1B ($^1T_2$).

The PL results for the $SrW_{(1-x)}Mo_xO_4$ samples show variations in behavior. These profiles can be associated with specific structural arrangements of the $[WO_4]$ or $[MoO_4]$ clusters. Moreover, the presence of two high frequencies is well evidenced in the Raman spectra referring to the bands at 887 cm^{-1} and 920 cm^{-1} for $SrMoO_4$ and $SrWO_4$ attributed to the symmetrical stretching of the connections [← O ← M → O →] (M = Mo and W), respectively. This is also similar for the $SrW_{(1-x)}Mo_xO_4$ solid solution. We consider that the differences in the PL intensity are related to the replacement of Mo^{6+} by W^{6+} in the $SrW_{(1-x)}Mo_xO_4$ solid solution, which may be correlated to the influence of chemical composition and electron transition.

The emission of PL from scheelite-type molybdates and tungstates is not fully understood. There are several strands which try to explain the photoluminescent behavior of these groups of materials. The PL properties can be caused by several possible mechanisms, and the spectra can be associated with different components. There are many aspects regarding an understanding of the PL behavior in the materials of molybdates and tungstates which have emerged and support their possible explanations of mechanisms. However, considering location, intensity and band displacement, all these aspects can be attributed to an intrinsic property of electronic charge transfer between different energy states within the $[WO_4]^{2-}/[MoO_4]^{2-}$ clusters, and the structural arrangement. These load transitions, energy states and structural arrangements are influenced by distortions in the $[WO_4]^{2-}/[MoO_4]^{2-}$ clusters. As mentioned, the coordination of clusters $[MO_x]$ also contributes to the charge transfer level between the 2p (O) and 5d (W) or 4d (Mo) orbitals [48].

The broadband profile in the photoluminescence spectra of $SrW_{(1-x)}Mo_xO_4$ sizes in Fig. 6 requires a multilevel emission mechanism, which represents an unqualified system or the execution of various methods involved in the participation of various factors involved within the material band gap. Similar behavior can be found in other materials [49]. Sczancoski et al. [50] relate the type of emission to the position of defects in the energy states of the band gap. The blue emission is attributed to surface defects (close to the valence band), useful for the O-2pσ orbital; on the other hand, a green emission is enabled for background defects (slightly away from the valence band) connected to the O-2pπ orbital [51]. According to Lei et al. [52] in relation to the complex principle $[MoO_4]^{2-}$, the coupling between the O-2pσ and O-2pπ orbitals and the *Mo-4d (t2)* and *Mo-4d* (*e*) orbitals is responsible for the hybridization of the molecular orbitals. Among these electron states, only the $^1A_1 \rightarrow {}^1T_2$ transition is allowed [53]. This attributes the blue emission to $^1A_1 \rightarrow {}^1T_2$ transition within $[MoO_4]^{2-}$ clusters for surface defects and green-orange emissions for defects in the MoO_3 group for deep defects [53]. The radiative emission process occurs more easily if there are trapped holes or trapped electrons within the band gap. In theoretical studies of $SrWO_4$ films, Orhan et al. [54] discovered that present distorted clusters $[WO_3]$ and $[WO_4]$ in the $SrWO_4$ trellis are very favorable to intermediate level surgery in the band gap range. The polarization that is favored due to the breaking of symmetry and the existence of these localized energy levels are favorable conditions for forming holes and trapped electrons.

Fig. 7 shows the deconvolutions of the photoluminescence emission spectra. The deconvolution curves are of the Gaussian type and represent how much (%) each component (color) contributes to the photoluminescent behavior as a whole. It is observed that the fit between the PL spectrum and the PL fitting is $R^2 = 0.999$. According to Santiago et al. [15], the emitted color is generated between the energy transfer from organized clusters, $[MoO_4]_o$, or to disorganized clusters, $[MoO_4]_d$. Variations in the colors emitted are observed due to the composition of $Mg_{1-x}Sr_xMoO_4$.

According to Oliveira et al. [55], the emission is attributed to the charge transfer between the O 2p orbital and the empty d orbital of the $[MO_4]^{2-}$ clusters (M = W and Mo), with excitation energies located within the gap. The only fundamental state associated with the Scheelite family is $^1A_1$ and the four excited states are ^1A ($^1T_1$), ^1E ($^1T_1$), ^1E ($^1T_2$) and ^1B ($^1T_2$) [56]. The different profiles in the PL spectra behavior are particularly related to the structural arrangement between the $[WO_4]$ or $[MoO_4]$ clusters. Other indications of structural disorder have previously been pointed out in XRD and Raman spectroscopy results.

It is possible to compare changes in the PL behavior as a function of the maximum displacement of the emission bands as a function of the compositional variation of the samples in Fig. S3. However, there was no significant reduction or increase in terms of emission intensity. Therefore, it is reasonable to consider that the effect of chemical composition influences energy-related characteristics of these materials, as well as the types and proportions of structural defects present.

Fig. 8 shows the chromaticity diagram, indicating the chromaticity coordinates with the digital photos of the presented emissions of $SrW_{(1-x)}Mo_xO_4$. It can be observed that the $SrWO_4$ sample shows emission in

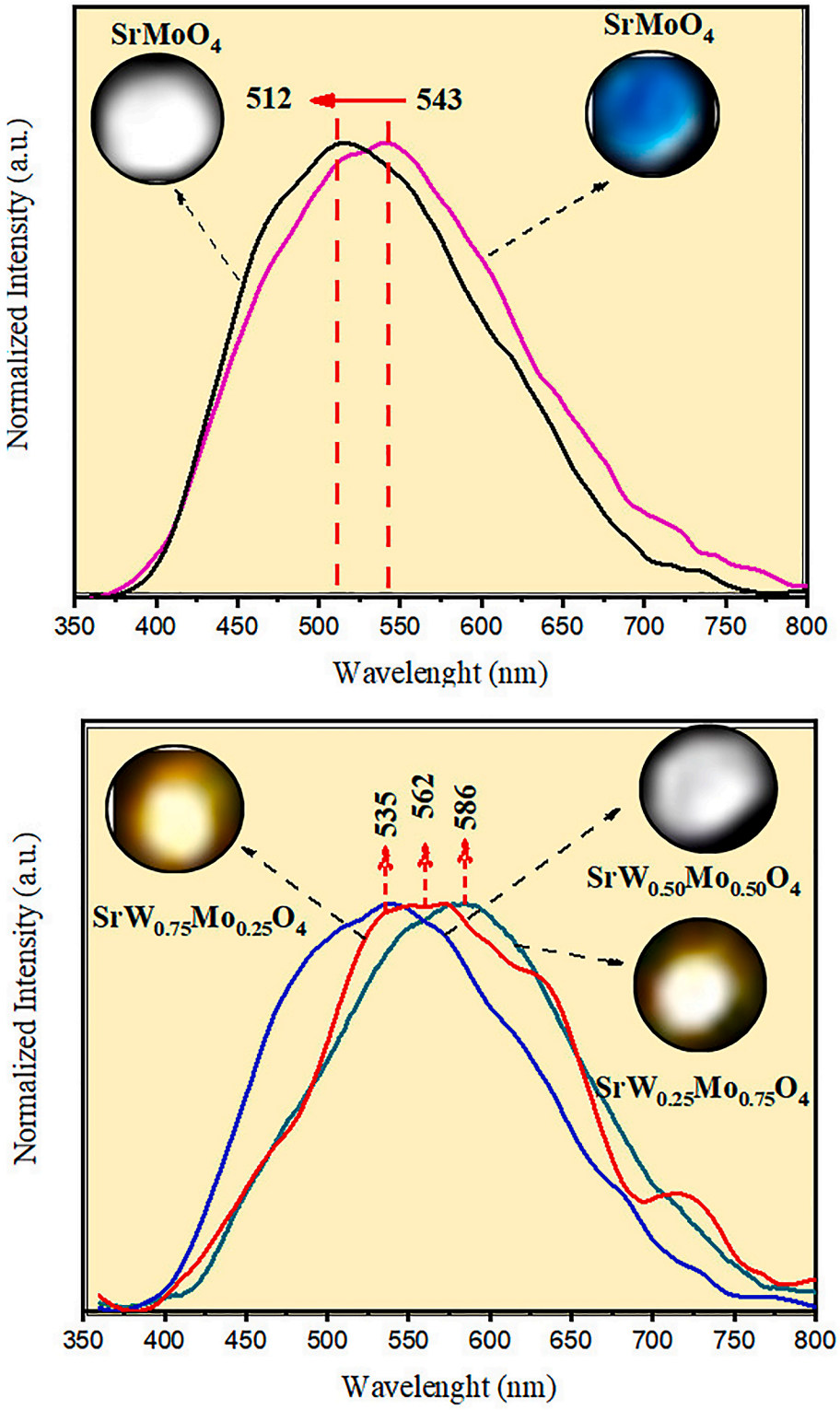

Fig. 6. Emission spectra of $SrW_{(1-x)}Mo_xO_4$ samples, λ_{exc} = 325 nm.

the blue region, having the greatest contribution in this region, as indicated in Fig. 7 (b). In contrast, the $SrMoO_4$ and $SrW_{0.5}Mo_{0.5}O_4$ samples show emission in the white region due to the adjustable contribution of simultaneous emissions in the blue, green and red regions, and the $SrW_{0.25}M_{0.75}O_4$ and $SrW_{0.75}M_{0.25}O_4$ samples exhibit yellow emissions. It appears that the characteristics of the emitted colors are modulated according to the chemical composition of $SrW_{(1-x)}Mo_xO_4$ samples. The gradual transition from $SrWO_4$ → $SrMoO_4$ goes through the following sequence: Blue → Yellow → White, together with the color quality parameters (CRI, CCT, LER).

The results of the color rendering index (CRI) obtained were in the range of 80–82%. The values indicate that the emissions ensure excellent reliability in the color integrity of the objects when illuminated by the produced samples. $SrMoO_4$ and $SrM_{0.5}W_{0.5}O_4$ samples have a white light source with high CCTs: 5478 and 5437 K, respectively. Fluorescent lamps have CCTs ranging from 3000 to 6500 K, while the CCT from the

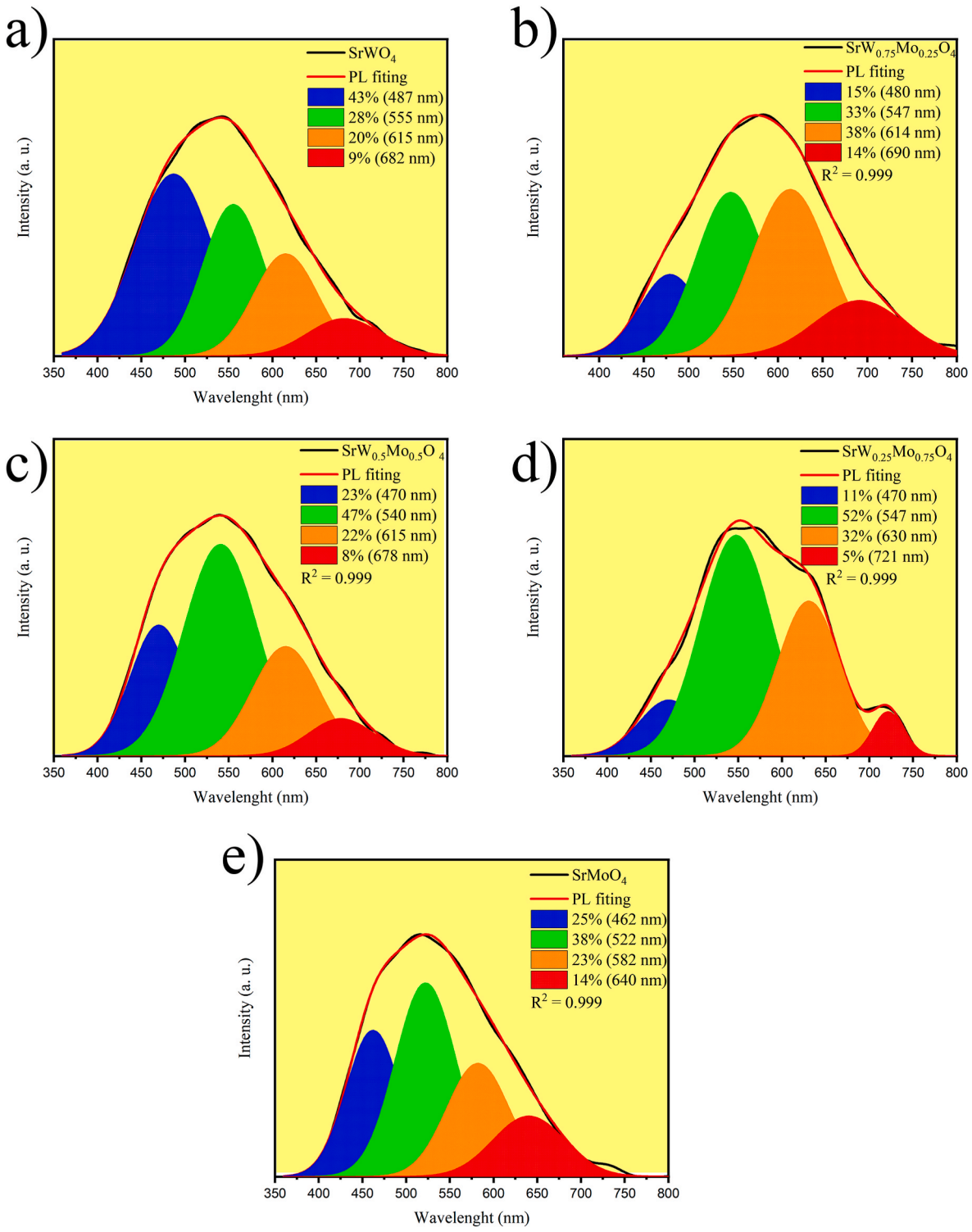

Fig. 7. Deconvolutions of the PL emission spectra of $SrW_{(1-x)}Mo_xO_4$.

sun is close to 6000 K [57].

The luminous efficiency of radiation (LER) of the samples was also investigated. The results revealed high LER values (322 $lm.W^{-1}$), a characteristic desired for use in WLEDs. The ratio of the emitted luminous flux in lumen and the power used in watts describes the LER. The LER is a measure expressed in lumens per visible watts used to estimate how brightly the radiation is perceived to be by the average human eye. The LER is determined by the spectral distribution S (λ) of the source, as given by Equation (5):

$$LER = \frac{Km \int_{360}^{830} V(\lambda)S(\lambda)d(\lambda)}{\int_{360}^{830} S(\lambda)d(\lambda)} \quad \text{Eq. (5)}$$

In which: $V(\lambda)$ = eye sensitivity curve and Km = 683 [l lm W^{-1}]], which is the highest possible efficiency that can ever be obtained from a light source [58]. Table 2 presents all the photometric parameters of the $SrW_{(1-x)}Mo_xO_4$ samples. The high values of LER and CRI indicate that the synthesized material has fundamental properties for applicability in

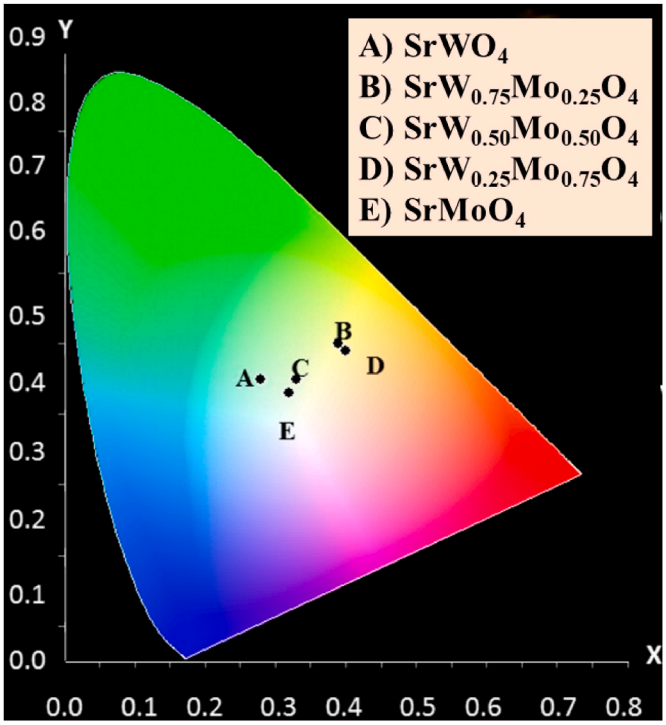

Fig. 8. Chromaticity diagram of $SrW_{(1-x)}Mo_xO_4$ samples.

WLEDs. Strong UV absorption is required to improve the CRI and LER photometric parameters to produce white light. Molybdates are gaining more and more attention in the reaserch field due to their strong visible light emission under excitation in UV [59]. Furthermore, molybdate and tungstate phosphors have excellent chemical stability and high luminous efficiency, constituting necessary characteristics for the development of solid-state lighting devices.

4. Conclusion

$SrW_{(1-x)}Mo_xO_4$ phosphors were successfully synthesized by the microwave-hydrothermal method. XRD patterns and the Rietveld refinement revealed that all samples have pure tetragonal phase, indicating the formation of solid solution. The structural parameters were observed and the Raman modes showed small changes due to the gradual substitution of $W^{6+} \rightarrow Mo^{6+}$ in the samples. The particles showed different morphologies according to the changes promoted in the chemical composition of the samples. The particle morphologies of $SrW_{(1-x)}Mo_xO_4$ show an evolution in their characteristics, presenting particles with micro-rice, microflower and microsphere forms. The particle formation is based on self-assembly and Ostwald ripening processes. The increase in the amount of W promotes the formation of spherical particles with a very porous surface. The emission in the white region was observed in the $SrMoO_4$ and $SrMo_{0.5}W_{0.5}O_4$ samples, which showed simultaneous emissions in the blue, green and red regions with a spectrum with a broadband profile. This photoluminescent behavior is related to specific structural arrangements of the $[WO_4]$ or $[MoO_4]$ clusters. The photometric parameter values of CRI (80%) and CCT (5478 and 5437 K) reveal that the $SrMoO_4$ and $SrW_{0.5}Mo_{0.5}O_4$ samples, respectively, are within what is expected for applications in WLEDs. The color of the white light source is investigated from these two properties. According to the results obtained in this study, the $SrW_{(1-x)}Mo_xO_4$ samples can be applied in solid-state lighting devices.

CRediT authorship contribution statement

L.X. Lovisa: interpretation of experimental data and writing of the article. **D.F. Dos Santos:** carrying out the experimental procedure. **A.A. G. Santiago:** structural refinement and article writing. **M. Siu Li:** carrying out photoluminescent measurements. **E. Longo:** provided the infrastructure for the characterization of the material. **M.R.D. Bomio:** provided the infrastructure for material characterizations and, Supervision. **F.V. Motta:** provided the infrastructure for material characterizations and, Supervision.

Declaration of competing interest

The authors declare that they have no known competing financial interests or personal relationships that could have appeared to influence the work reported in this paper.

Data availability

The data that has been used is confidential.

Acknowledgements

The authors wish to thank the financial support of the following Brazilian research funding agencies: the National Council for Scientific and Technological Development (*CNPq*), the Coordination for the Improvement of Higher Education Personnel (*CAPES*) and the Graduate Program in Materials Science and Engineering (*PPGCEM/UFRN*).

Appendix A. Supplementary data

Supplementary data to this article can be found online at https://doi.org/10.1016/j.optmat.2022.113166.

References

[1] Q. Liu, F. Meng, X. Zhang, et al., Al^{3+}-doping-induced enhancement of $Tb_3Ga_5O_{12}$:Eu^{3+} Orange light-emitting phosphor photoluminescence for white light-emitting diodes, J. Lumin. 226 (2020), 117505.
[2] J. Xuea, H. Mi Noh, B.C. Choia, et al., Dual-functional of non-contact thermometry and field emission displays via efficient Bi3+ → Eu3+ energy transfer in emitting-color tunable GdNbO4 phosphors, Chem. Eng. J. 382 (2020), 122861.
[3] Y. Hua, Y.-U. Seo, S.Y. Kim, H.-J. Kim, J.S. Yu, Rare-earth-free $Sr_2YSb_{1-x}O_6$:xMn^{4+}: synthesis, structure, luminescence behavior, thermal stability, and Applications, Chem. Eng. Sci. 412 (2021), 128633.
[4] B. Zhang, J. Zhang, Y. Guo, et al., Zhang, Synthesis and photoluminescence of double perovskite La_2LiSbO_6:Ln^{3+} (Ln= Eu, Tb, Tm, Sm, Ho) phosphors and enhanced luminescence of La_2LiSbO_6:Eu^{3+} red phosphor via Bi^{3+} doping for white light emitting diodes, J. Alloys Compd. 787 (2019) 1163–1172.
[5] Y. Hua, J.S. Yu, Emission enhancement of bifunctional La_2MoO_6:Sm^{3+} nanoparticles by doping Y^{3+} ions for flexible display and high CRI WLEDs, J. Alloys Compd. 820 (2020), 153162.
[6] Y. Shimizu, Japanese Patent Application Publication H08-7614, 1996.
[7] Y. Shimizu, K. Sakano, Y. Noguchi, T. Moriguchi, Japanese Priority Patent Applications to U. S. Patent 5, vol. 998, 1996, p. 925.
[8] in Japanese K. Bando, Y. Noguchi, K. Sakano, Y. Shimizu, Tech. Digest, Phosphor Res. Soc. 264th Meeting, November 29, 1996.
[9] N.S. Shimbun, White LED lamp: light emission with high luminous efficiency halving production costs, in: The Japanese Newspaper Nikkei Sangyo Shimbun, Nikkei Industrial Journal, 1996.
[10] L. Sun, B. Devakumar, J. Liang, S. Wang, Q. Sun, X. Huang, A broadband cyan-emitting $Ca_2LuZr_2(AlO_4)_3$:Ce^{3+} garnet phosphor for near-ultraviolet-pumped warm-white light-emitting diodes with an improved color rendering index, J. Mater. Chem. C 8 (2020) 1095–1103.
[11] U. Farooq, Z. Zhao, Z. Sui, et al., Tm^{3+}/Dy^{3+}/Eu^{3+} (Sm^{3+}) tri-activated Y_2WO_6 as one potential single-phase phosphor for WLEDs, J. Alloys Compd. 778 (2019) 942–950.
[12] U.B. Humayoun, S.B. Kwon, S.K. Sami, D.-H. Yoon, $(NH_4)_3AlF_6$:Mn^{4+} a novel red phosphor e facile synthesis, structure and luminescence characteristics, J. Alloys Compd. 776 (2019) 594–598.
[13] H. Orücü, S. Tabanli, M. Erdem, Y. Oztürk, G. Eryürek, Bright white light up-conversion luminescence from Yb^{3+}/Er^{3+}/Tm^{3+} tridoped gadolinium gallium garnet nano-crystals for multicolor and white light-emitting diodes, Opt. Mater. 131 (2022), 112613.
[14] I. Levchuk, A. Osvet, C.J. Brabec, M. Batentschuk, A. Shakhno, T. Zorenko, Y. Zorenko, Micro-powder $Ca_3Sc_2Si_3O_{12}$:Ce silicate garnets as efficient light converters for WLEDs, Opt. Mater. 107 (2020), 109978.

[15] A.A.G. Santiago, R.L. Tranquilin, P. Botella, et al., Spray pyrolysis synthesis and characterization of $Mg_{1-x}Sr_xMoO_4$ heterostructure with white light emission, J. Alloys Compd. 813 (2020), 152235.

[16] H. Yu, X. Shi, L. Huang, X. Kang, D. Pan, Solution-deposited and low temperature-annealed Eu^{3+}/Tb^{3+}-doped $CaMoO_4/SrMoO_4$ luminescent thin films, J. Lumin. 225 (2020), 117371.

[17] X. Liu, J. Wang, R. Lei, S. Zhao, F. Huang, D. Deng, S. Xu, Comparison study on the different strategies designed for ratiometric luminescence thermometry in Er^{3+}/Yb^{3+}: $SrMoO_4$ phosphor, Sensor. Actuator. 315 (2020), 112287.

[18] N. Najafvandzadeh, S. López-Moreno, D. Errandonea, P. Pavone, C. Drax, First-principles study of elastic and thermal properties of scheelite-type molybdates and tungstates, Mater. Today Commun. 24 (2020), 101089.

[19] V. Chauhan, P.K. Pandey, P. Dixit, P. Deshmukh, S. Satapathy, P.C. Pandey, Effect of Zn^{2+} co-doping on the luminescence of Sm^{3+} doped $SrMoO_4$ phosphor, J. Lumin. 248 (2022), 118994.

[20] Q. Li, Z. Zhao, X. Bai, X. Tong, et al., Tunable and stable localized surface plasmon resonance in $SrMoO_4$ for enhanced visible light driven nitrogen reduction, Chin. J. Catal. 42 (2021) 1763–1771.

[21] D.F. Dos Santos, L.X. Lovisa, A.A.G. Santiago, , et al.F.V. Motta, Growth mechanism and vibrational and optical properties of $SrMoO_4$: Tb^{3+}, Sm^{3+} particles: green-orange tunable color, J. Mater. Sci. 55 (2020) 8610–8629.

[22] X. Liu, J. Wang, R. Lei, S. Zhao, F. Huang, D. Deng, S. Xu, Comparison study on the different strategies designed for ratiometric luminescence thermometry in Er3+/Yb3+: SrMoO4 phosphor, Sens. Actuators, A 315 (2020), 112287.

[23] E.O. Gomes, L. Gracia, A.A.G. Santiago, et al., Structure, electronic properties, morphology evolution, and photocatalytic activity in PbMoO4 and Pb1-2*x*Ca*x*Sr*x*MoO4 (x = 0.1, 0.2, 0.3, 0.4 and 0.5) solid solutions, Phys. Chem. Chem. Phys. 22 (2020), 25876.

[24] P.F.S. Pereira, A.F. Gouveia, M.M. Ferrer, et al., α-Ag2-2*x*Zn*x*WO4 ($0 \leq x \leq 0.25$) solid solutions: structure, morphology, and optical properties, Inorg. Chem. 56 (2017) 7360–7372.

[25] A.K. Sonia, R. Joshia, K. Jangid, R. Tewarid, R.S. Ningthoujam, Low temperature synthesized $SrMoO_4$:Eu^{3+} nanophosphors functionalized with ethylene glycol: a comparative study of synthesize route, morphology, luminescence and annealing Mater, Res. Bull. 103 (2018) 1–12.

[26] B.H. Toby, EXPGUI, a graphical user interface for GSAS, J. Appl. Crystallogr. 34 (2001) 210–213.

[27] K. Momma, VESTA 3 for three-dimensional visualization of crystal, volumetric and morphology data, J. Appl. Crystallogr. 44 (2011) 1272.

[28] L.X. Lovisa, D.F. Dos Santos, A.A.G. Santiago, et al., Enhanced red emission in $Sr_{(1-x)}Eu_xMo_{0.5}W_{0.5}O_4$ (x = 0.01, 0.02, 0.04) phosphor and spectroscopic analysis for display applications, J. Mater. Sci. 57 (2022) 8634.

[29] T.T. Basiev, Y.K. Voronko, P.G. Zverev, Spontaneous Raman spectroscopy of tungstate and molybdate cryystals for Ramn lasers, Opt. Mater. 15 (2000) 205.

[30] T. Wu, Y. Lu, L. Wei, H. Gaoa, Morphology-controlled synthesis, characterization, and luminescence properties of $KEu(MoO_4)_2$ microcrystals, CrystEngComm 15 (2013) 2761.

[31] W. Xia, S. Hu, J. Xiong, J. Tang, J. Yan, Self-assembled hierarchical architecture of tetragonal $AgLa(MoO_4)_2$ crystals: hydrothermal synthesis, morphology evolution and luminescence properties, CrystEngComm 20 (2018) 1832.

[32] X. Ren, Y. Zhang, Q. Li, M. Yu, Sodium citrate (Na_3Cit)-assisted hydrothermal synthesis of uniform spindle-like $SrMoO_4$:Eu^{3+} phosphors, Mater. Res. Bull. 59 (2014) 283–289.

[33] Y. Cao, D. Ji, Phase- and shape-controlled hydrothermal synthesis of CdS nanoparticles, and oriented attachment growth of its hierarchical architectures, Appl. Surf. Sci. 265 (2013) 771.

[34] Y. Zhou, B. Yan, Self-assembled $RE_2(MO_4)_3$:Ln^{3+} (RE = Y, La, Gd, Lu; M = W, Mo; Ln = Yb/Er, Yb/Tm) hierarchical microcrystals: hydrothermal synthesis and up-conversion luminescence, Opt. Mater. 36 (2014) 602.

[35] D.A. Spassky, I.A. Kamenskikh, V.V. Mikhailin, A.E. Savon, Y.A. Hizhnyi, S. G. Nedilko, P.A. Lykov, Electronic structure and luminescence mechanisms in $ZnMoO_4$ crystals, J. Phys. Condens. Matter Inst. Phys. 23 (2011), 365501.

[36] P.S. Dutta, A. Khanna, Eu^{3+} activated molybdate and tungstate based red phosphors with charge transfer band in blue region, ECS J. Solid State Sci. Technol. 2 (2012) R3153–R3167.

[37] P. Kubelka, Ein beitrag zur optik der farbanstriche, Zeitschrift fur Technische Physik 12 (1931) 593.

[38] A.E. Morales, E.S. M, U. Pal, Use of diffuse reflectance spectroscopy for optical characterization of un-supported nanostructures, Rev. Mexic. Fisica 56 (2007) 18.

[39] D.K. Ferry, Semiconductors Bonds and Bands, first ed., IOP ebooks, United Kingdom, 2013.

[40] Y. Zhang, R.T. Williams, Electronic band structures of the scheelite materials CaMoO4, CaWO4, PbMoO4, and PbWO4, Phys. Rev. B 57 (1998), 12738.

[41] B. Li, A.Y. Lan, H.X. Tang, One-dimensional $CdWO_4$:Tb^{3+} nanofibers: electrospinning fabrication and luminescence, Chem. Phys. Lett. 636 (2015) 22.

[42] W.S. Wang, C.-Y. Xu, W.-Z. Shao, Room temperature synthesis, growth mechanism, photocatalytic and photoluminescence properties of cadmium molybdate core-shell microspheres, Cryst. Growth Des. 9 (2009) 1558.

[43] D. Li, Z. Nie, L. Zhang, Y. Bai, X. Zhang, Y. Song, Y. Wang, Anomalous upconversion luminescence of $SrMoO_4$:Yb^{3+}/Er^{3+} nanocrystals by high excited state energy transfer, J. Alloys Compd. 650 (2015) 799.

[44] L. Chen, Y. Gao, Mechanisms and applications of cell electrochemical technique to prepare luminescent $SrMoO_4$ thin films, Chem. Eng. J. 131 (2007) 181.

[45] M.C. Oliveiraa, et al., Geometry, electronic structure, morphology, and photoluminescence emissions of $BaW_{1-x}Mo_xO_4$ (x=0, 0.25, 0.50, 0.75, and 1) solid solutions: theory and experiment in concert, Appl. Surf. Sci. 463 (2019) 907.

[46] A. Phuruangrat, S. Thongtem, Precipitate synthesis of $BaMoO_4$ and $BaWO_4$ nanoparticles at room temperature and their photoluminescence properties, Superlattice. Microst. 52 (2012) 78.

[47] Z. Gao, W. Sun, Y.-H. Hu, X.W. Liu, T. Nonferr, Surface energies and appearances of commonly exposed surfaces of scheelite crystal, Metal. Soc. 23 (2013) 2147.

[48] V.S. Marques, J.C. Sczancoski, A.F.P. Alcantara, et al., Effect of different solvent ratios(water/ethylene glycol) on the growth process of $CaMoO_4$ crystals and their optical properties, Cryst. Growth Des. 10 (2010) 4752.

[49] D.F. Dos Santos, et al., Growth mechanism and vibrational and optical properties of $SrMoO_4$: Tb^{3+}, Sm^{3+} particles: green-orange tunable color, J. Mater. Sci. 55 (2020) 8610.

[50] J.C. Sczancoski, et al., Electronic structure and optical properties of $BaMoO_4$ powders, Curr. Appl. Phys. 10 (2010) 614–624.

[51] V.M. Longo, L.S. Cavalcante, R. Erlo, et al., Strong violet-blue light photoluminescence emission at room temperature in $SrZrO_3$: joint experimental and theoretical study, Acta Mater. 56 (2008) 2191.

[52] M. Lei, et al., Controllable route to barium molybdate crystal and their photoluminescence, J. Alloys Compd. 639 (2015) 102.

[53] A. Xie, X. Yuan, S. Hai, et al., Enhancement emission intensity of $CaMoO_4$: Eu^{3+}, Na^+ phosphor via Bi co-doping and Si substitution for application to white LEDs, J. Phys. D Appl. Phys. 42 (2009), 105107.

[54] E. Orhan, et al., Conditions giving rise to intense visible room temperature photoluminescence in $SrWO_4$ thin films: the role of disorder, Chem. Phys. 312 (2005) 1.

[55] M.C. Oliveira, J. Andrés, L. Gracia, et al., Geometry, electronic structure, morphology, and photoluminescence emissions of $BaW_{1-x}Mo_xO_4$ (x=0, 0.25, 0.50, 0.75, and 1) solid solutions: theory and experiment in concert, Appl. Surf. Sci. 463 (2019) 907–917.

[56] T. Thongtem, A. Phuruangrat, S. Thongtem, Synthesis of $CaWO_4$, $SrWO_4$ and $BaWO_4$ with nanosized particles using cyclic microwave radiation, J. Ceram. Process. Res. 9 (2008) 258–261.

[57] E.F. Schubert, Light-emitting Diodes, Cambridge University Press, New York, 2006.

[58] P.F. Smet, A.B. P, D. Poelman, Selecting conversion phosphors for white lightemitting diodes, J. Electrochem. Soc. 158 (2011) R37.

[59] X. Liu, L. L, H.M. Noh, B.K. Moon, B.C. Choi, J.H. Jeong, Chemical bond properties and charge transfer bands of O^2-Eu^{3+}, O^{2-}-Mo^{6+} and O^2-W^{6+} in Eu^{3+}-doped garnet hosts $Ln_3M_5O_{12}$ and ABO_4 molybdate and tungstate phosphors, Dalton Trans. 43 (2014) 8814.